Colloids and Surfaces A: Physicochemical and Engineering Aspects 726 (2025) 137761

Contents lists available at ScienceDirect

Colloids and Surfaces A: Physicochemical and Engineering Aspects

journal homepage: www.elsevier.com/locate/colsurfa

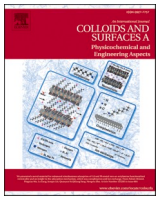

Size-tunable gold nanosphere superlattices with enhanced SERS performance

Jia-Fei Gao [a], Jie Liu [a,*], Gui-Lin Wu [a], Kun-Peng Wang [a], Yiqiang Gao [a,*], Tian-Song Deng [a,b,**]

[a] School of Electronics and Information Engineering, Hangzhou Dianzi University, Hangzhou 310018, China
[b] Key Laboratory of Micro-nano Sensing and IoT of Wenzhou, Wenzhou Institute of Hangzhou Dianzi University, Wenzhou 325038, China

HIGHLIGHTS

- Synthesis of monodisperse gold nanospheres larger than 65 nm (68, 91, 114 nm).
- Gas-liquid interface self-assembly for large-area ordered gold nanosphere monolayers.
- Optical property characterization and SERS performance analysis of superlattices.

GRAPHICAL ABSTRACT

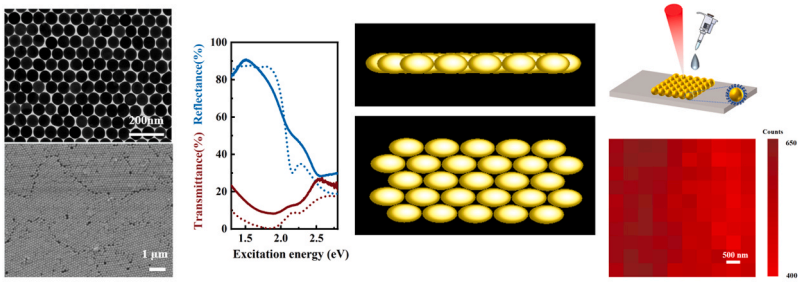

ARTICLE INFO

Keywords:
Gold nanospheres
Superlattice
Localized surface plasmon resonance
Self-assembly
SERS

ABSTRACT

Nanoparticle superlattices of varying sizes are of great significance for applications in electronic and plasmonic devices, as well as optical metasurfaces. In this study, large-sized gold nanospheres were synthesized through a seed-mediated method, and then functionalized with thiol group. Large-area monolayer superlattices were then self-assembled at the liquid -liquid interface. By varying the seed concentration, gold nanospheres with tunable diameters and ultra-smooth surfaces were obtained. The optical properties of these superlattices were investigated through reflectance and transmittance measurements, along with finite-difference time-domain (FDTD) simulations. The monolayer superlattices can be served as high-sensitivity Surface-Enhanced Raman Scattering (SERS) platforms, exhibiting a high density of electric field hotspots. As the particle size increased, the intensity of localized surface plasmon resonance (LSPR) also enhanced. Additionally, the influence of laser excitation wavelength and probe molecule types and concentrations on SERS response, were investigated. A direct correlation was observed between SERS intensity and probe molecule concentration across five orders of magnitude. Finally, these monolayer superlattices proved to be reproducible and uniformly enhanced substrates, widely applicable in sensing technologies.

* Corresponding authors.
** Corresponding author at: School of Electronics and Information Engineering, Hangzhou Dianzi University, Hangzhou 310018, China.
E-mail addresses: liujie4209@hdu.edu.cn (J. Liu), yqgao@hdu.edu.cn (Y. Gao), dengts@pku.edu.cn (T.-S. Deng).

https://doi.org/10.1016/j.colsurfa.2025.137761
Received 11 April 2025; Received in revised form 18 June 2025; Accepted 15 July 2025
Available online 16 July 2025

1. Introduction

Nanoparticle superlattices are periodic arrays composed of nanoscale building blocks, such as metal nanoparticles, quantum dots, and magnetic nanoparticles. Compared to individual nanoparticles or their corresponding bulk materials, nanoparticle superlattices exhibit unique collective properties, such as enhanced electrical, optical, and magnetic behaviors that surpass those observed in isolated particles or bulk materials [1,2]. Superlattices can be classified into single crystal superlattices [3–8], binary superlattices [9–12], and multi-component superlattices, depending on the types of constituent nanoparticles. Since single crystal superlattices are composed of only one type of nanoparticle, their preparation process is simpler, easier to control, and more reproducible. They also exhibit high structural order, significantly reducing lattice defect density and ensuring the formation of high-quality superlattices.

Over the past decade, various shapes of noble metal nanoparticles have been synthesized and assembled into single crystal superlattices, such as gold nanorods [5], gold nanobipyramids [6,8], gold nanocubes, and gold nanospheres [7,13]. Among these, gold nanospheres have been widely used in superlattice assembly due to their geometric symmetry, tunable optical properties, and ease of preparation through wet chemical methods [14–16].

Small gold nanoparticles exhibit significant localized surface plasmon resonance (LSPR) in the visible light region, resulting in strong absorption and scattering capabilities, making them suitable for absorbing short-wavelength light. They demonstrate excellent performance in biological imaging and sensing applications, as their limited near-field effects lead to pronounced enhancement. In contrast, as particle size increases, the LSPR peak redshifts toward longer wavelengths, giving rise to higher-order plasmon modes (e.g. quadrupole modes), which enhance optical properties at specific wavelengths. Additionally, strong interparticle interactions and nanoscale gap effects in larger gold nanoparticle assemblies generate intense local electric fields, amplifying light-matter interactions. These characteristics make large gold nanoparticles particularly valuable for surface-enhanced Raman scattering (SERS) applications [17–19].

For gold nanospheres (diameter <65 nm), various single-layer, multi-layer, and multi-layer crystal superlattices have been reported and extensively studied in terms of their structural, electronic, and optical properties [2,10,20–24]. Well-defined plasmonic polarization is observed in gold nanospheres with diameters of at least ~25 nm [12,25,26]. In bi-layer and tri-layer superlattices of composed of ~46 nm gold nanospheres, dark plasmon modes are excited. As the number of layers increases, these dark modes transformed into standing waves that facilitate light transmission through the superlattice [12].

However, for large gold nanospheres (>65 nm), achieving high uniformity in size and shape is challenging. Additionally, self-assembly of large nanospheres is hindered by increased interparticle repulsion and defect formation, making it difficult to maintain the stability and structural order of large-area superlattices. As a result, research on the self-assembly of monolayer superlattices with large gold nanospheres remains limited, and their optical properties, SERS performance, and other aspects require further exploration.

For large gold nanospheres (diameter >65 nm), achieving high uniformity in size and shape remains a significant challenge. In recent years, researchers have developed various advanced assembly strategies, including liquid-liquid interface assembly, DNA-mediated directed assembly, instant interfacial self-assembly, and three-phase interfacial self-assembly [27–29]. However, as the nanoparticle size increases, interparticle repulsion becomes stronger and defects are more likely to form, hindering the ordered self-assembly process and making it difficult to obtain large-area, highly ordered, and stable superlattices. Therefore, research on the construction of monolayer superlattices composed of large gold nanospheres remains limited, and their optical response properties, SERS performance, and related structure-property relationships require further systematic investigation.

In this study, we present a simple and convenient strategy for assembling large gold nanospheres (diameter >65 nm) into highly ordered, periodically arranged superlattices over large area. Using a seed-mediated growth method combined with mild oxidation, we synthesized large, uniform gold nanospheres with smooth surfaces and high monodispersity, with diameter precisely controlled by the initial seed concentration. The gold nanospheres were then functionalized with PS-SH, forming a hydrophobic polystyrene (PS) layer that provided long-term dispersion stability in organic solvents. The superlattices were assembled at the liquid-liquid interface, resulting in superlattices with minimal defects. We systematically investigated the optical properties of the assembled large-sized gold nanosphere superlattices through reflectance, transmittance, and absorbance measurements. More importantly, these superlattices exhibited excellent surface-enhanced Raman scattering (SERS) performance, successfully creating efficient and stable SERS substrates. By finely tuning and optimizing the self-assembled nanostructures, we achieved highly sensitive detection under extremely low probe molecule concentrations and ultra-low laser power conditions. Compared to conventional SERS tests with high concentrations and high-power consumption, our approach significantly reduces background noise and energy consumption [30,31]. This breakthrough not only meets the stringent requirements of practical applications for low power consumption, low background noise, and high sensitivity but also fills the gap in performance optimization of large gold nanosphere superlattices in the SERS field, highlighting the important innovations and promising applications of this research in nanoparticle assembly and functionalization.

2. Results and discussion

To synthesize large-sized, highly uniform, gold nanoparticles with smooth surfaces, we employed the seed mediated growth method proposed by Ruan et al. [15]. Firstly, small AuNSs with uniform morphology and high monodispersity were prepared. The colloidal solution of these small AuNSs appeared wine red, with an average diameter of 23.9 nm and a standard deviation of 1.7 nm. Their size distribution was narrow and followed a Gaussian curve (Fig. S1). Larger AuNSs were obtained through the overgrowth and mild oxidation of the smaller AuNSs. As a general trend, the final nanoparticle diameter was controlled by the initial seed concentration. When the amount of small gold nanoparticles added was changed from 0.5 mL, 0.2 mL, to 0.1 mL, the corresponding AuNS diameters increased from 68.0 ± 2.6 nm, to 91.1 ± 4.2 nm, and 114.6 ± 2.5 nm, respectively (Fig. S2, Fig. S3). To analyze the optical properties of these AuNSs, UV–vis spectroscopy was performed. The measured extinction spectra revealed that as the nanoparticle diameter increased, the dipolar plasmonic mode gradually redshifted from 537 nm to 573 nm. This phenomenon arises from the combined effects of several physical mechanisms. First, the larger particle size leads to stronger dipole coupling between neighboring nanospheres, significantly enhancing the gap effect and localizing the electromagnetic field in the gaps, which shifts the plasmon resonance to longer wavelengths. Second, radiation damping and radiation loss become more pronounced for larger particles, leading to greater energy dissipation via radiation and contributing to the redshift. Additionally, phase retardation occurs as electromagnetic waves propagate through the larger nanospheres, and higher-order multipolar modes (such as quadrupole and octupole modes) start to play a significant role in the optical response. These higher-order modes resonate at longer wavelengths than dipolar modes, further driving the redshift. Additionally, due to the greater radiation loss in larger AuNSs, the LSPR bandwidth was observed to broaden progressively.

To facilitate superlattice formation, the AuNSs were surface-functionalized with polystyrene-thiol (PS-SH), leveraging the strong affinity of thiol groups for gold surfaces. This modification enabled smaller particle gaps, resulting in densely packed alkyl chains and a

single-layer superlattice with an all trans conformation. UV–vis extinction spectroscopy (Fig. S4) indicated a slight redshift, which was attributed to two key factors. One is formation of strong Au-S bonds by PS-SH molecules, which modified the surface charge density and altered the surface plasmon resonance frequency. The other is changes in the refractive index (n) of the surrounding medium. The relationship between the refractive index and the optical dielectric constant (ε) of the external medium (solvent, carrier, or surfactant) follows:

$$n = \varepsilon^{1/2} \quad (1)$$

In the case of toluene ($\varepsilon = 2.24$), the increased refractive index leads to a decreased resonance frequency compared to water ($\varepsilon = 1.33$) [32].

To further verify the success of surface modification of gold nanoparticles, we conducted oil-water separation experiments and energy-dispersive X-ray spectroscopy (EDS) analysis. In the oil-water separation experiment, before functionalization, AuNS@CTAB was hydrophilic, making them easily dispersible in aqueous phase. After functionalizing with PS-SH, the CTAB on the AuNS surface was replaced by PS-SH. The surface chemical properties of AuNSs were changed, resulting in AuNS@PS-SH more lipophilic and easily dispersed in toluene (oil phase) (Fig. S5). In the EDS analysis, Fig.S6a presents the high-angle annular dark-field scanning transmission electron microscopy (HAADF-STEM) image of the modified AuNS, while Fig.S6b–c display the corresponding EDS elemental maps, where blue represents Au and red represents S. The sulfur element is predominantly distributed on the surface of AuNS, indicating a large-scale replacement of the CTAB bilayer. In summary, the introduction of PS-SH successfully altered the surface chemical properties of AuNS, enabling their effective transfer from the aqueous phase to the organic phase.

Next, a two-dimensional (2D) superlattice was fabricated using individual AuNSs as building blocks and combined with liquid -liquid interface self-assembly technology. The superlattice preparation process is illustrated in Fig. 1, using the method described by Dong et al. [33]. with slight modification. The toluene solution of AuNS@PS-SH was concentrated, and transferred onto the DEG subphase contained within a polytetrafluoroethylene trough. Then the trough was covered with a glass slide to slow down the evaporation of toluene. Superlattice monolayer thin films are usually formed after 24 h. The monolayer film was prepared on a substrate sized 1.5 cm × 1.5 cm, with a coverage area of approximately 0.5 cm^2 and good uniformity (Fig. S7). This film could then be transferred onto various substrates, such as copper grids, silicon wafers, and quartz glass, for further characterization and applications.

Fig. 2 shows the periodic arrangement, low defect density, and large-area single-layer superlattices assembled from PS-SH modified AuNSs

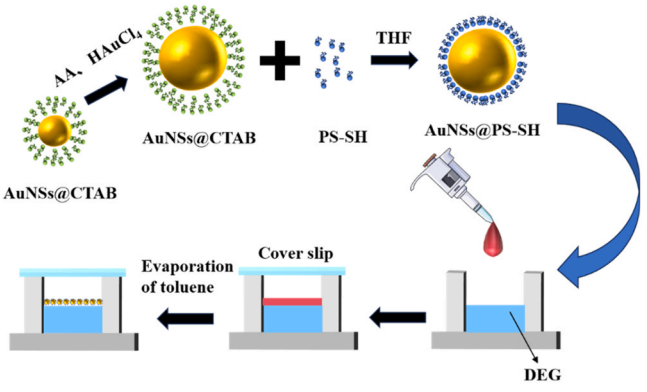

Fig. 1. Preparation scheme for AuNS superlattices at liquid -liquid interface. Firstly, using small gold nanospheres were used as the seed solution to synthesize larger gold nanospheres, which were subsequently functionalized with PS-SH ligands, forming AuNS@PS-SH nanospheres. Then, 100 μL of AuNS@PS-SH solution was transferred via pipette and gently dropped onto the DEG subphase. The mold was covered with a glass slide to slow down the toluene evaporation. After 16–24 h, a uniform monolayer superlattice was formed on the surface of DEG.

with different diameters. When the superlattices were transferred onto the substrate, external mechanical stress induces stress concentration, leading to the formation of cracks in the superlattices structure (Fig. 2 and Fig.S8). The gaps between adjacent nanoparticles in the superlattices were analyzed using ImageJ software, and the results are shown in Fig. S9: The superlattice assembled from gold nanoparticles with a diameter of 68 nm had a gap of 3.0 ± 1.8 nm (Fig. S9a); when the diameter of the gold nanoparticles increased to 91 nm, the gap in the superlattice decreased to 1.2 ± 1.5 nm (Fig. S9b); and when the diameter further increased to 114 ± 0.7 nm, the gap was further reduced to 0.6 ± 0.7 nm (Fig. S9c). These variations in particle gaps reflect the impact of the size of the gold nanoparticles on the superlattice structure and arrangement, with an increase in particle size leading to a gradual reduction in the superlattice gap.

To investigate the effect of particle diameter on the optical properties of these superlattices, we transferred them onto quartz substrates and studied their optical properties through optical microscopy and spectroscopy.

Fig. 3a presents the measured and simulated absorption spectra of a single-layer superlattice assembled from AuNSs with a diameter of 68 nm. Its characteristic is a weak peak at 2.1 eV, attributed to a bright plasmon mode where all dipoles oscillate in phase [12].

For the AuNS@91 nm and AuNS@114 nm superlattices, more pronounced spectral variations were observed (Fig. 3b, c). Distinct reflection valleys and absorption peaks appeared at 1.72 eV, resulting from the smaller gaps within the superlattice and the larger particle diameter, which lead to the excitation of plasmon polarized excitons. By measuring the reflectivity (R) and transmittance (T) of the superlattice, the absorption rate (A) could be calculated using the law of conservation of energy to determine its absorption rate ($A = 1 - R - T$) [34]. The obtained absorption rate of AuNS@91 nm was shown in Fig. S10a, and a clear absorbance peak appeared at 1.72 eV. Figure S10b the simulated absorbance results for AuNS@91 nm, which is highly consistent with the experimental data. As AuNS diameter increased, the intensity of light-matter coupling also increased, resulting in a gradual redshift of both the reflection valley and transmission peak. In addition, when the AuNS diameter was larger, the decrease in reflection became more pronounced. Each decrease in reflectivity is accompanied by a maximum transmittance. When the excitation energy exceeded 2 eV, the interband transition effect of gold significantly increased the absorption of the superlattice, causing a steep decrease in reflectivity [12,26].

To further interpret the experimental results, we simulated the reflectivity and emissivity of hexagonal close packed (hcp) single-layer gold nanoparticles using finite-difference time-domain (FDTD) method (dashed lines in Fig. 3a, b, c) [35]. The experimental measurements are in good agreement with the FDTD simulation results. This indicates that nanoparticle size and spacing were precisely controlled during the preparation process. The resulting optical properties matched the expected plasmonic behavior, confirming the accuracy of the fabrication process.

The numerous hotspots in the gaps between particles within the superlattice make the AuNS superlattices highly promising for surface enhanced Raman scattering (SERS) applications [8,36–39].

To investigate the effect of AuNS size on SERS signals, Raman spectroscopy tests were conducted on the superlattices assembled from AuNSs with different diameters. Firstly, the prepared superlattice was transferred onto a silicon wafer, and 10 μL Nile red dye solution (10^{-8} M) was added dropwise. The sample was then irradiated with a 633 nm laser (Fig. 4a). Nile Red was selected as an analyte probe because of its lipophilicity and distinct Raman peak at 592 cm^{-1} [40].

We plotted the SERS intensity map of Nile Red at 592 cm^{-1}, with a laser power of 1 % and an exposure time of 1 s, under one accumulation (Fig. 4b, c, d). The SERS intensity distribution, represented by color variations, indicated uniform enhancement across the superlattice. These results suggest that the AuNS superlattice exhibited highly uniform Raman response with minimal spatial variation.

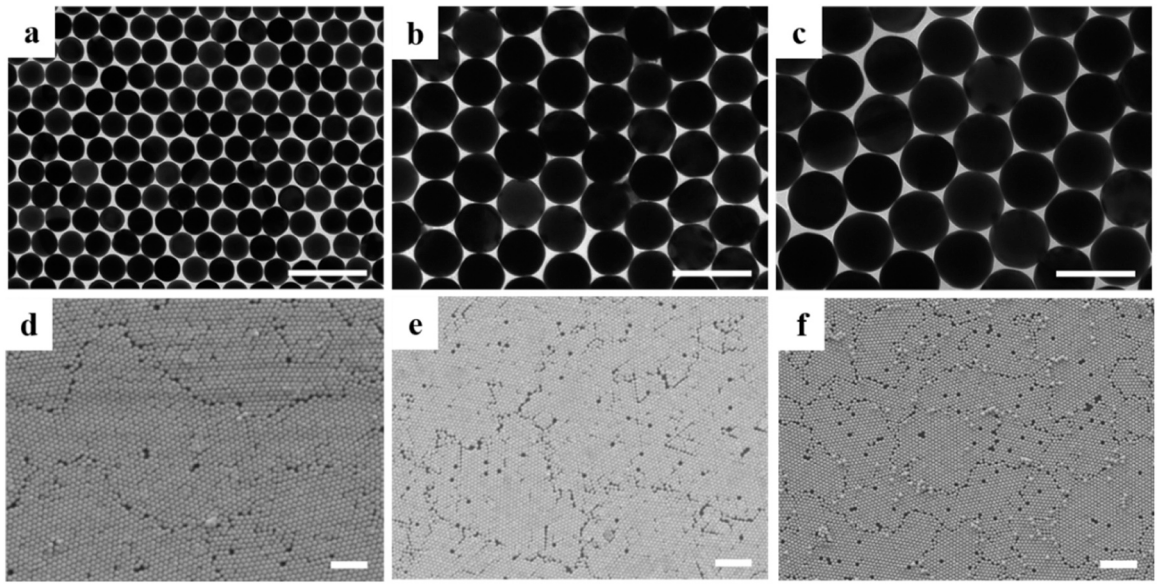

Fig. 2. TEM (top row) and SEM (bottom row) images of monolayer superlattice samples formed by gold nanospheres of different sizes (a, d) 68.0 ± 2.6 nm. (b, e) 91.1 ± 4.2 nm. (c, f) 114.6 ± 2.5 nm. The images illustrate the uniformity and hexagonal close-packed arrangement of the nanoparticle superlattices. TEM scalebar: 200 nm; SEM scalebar: 1 μm.

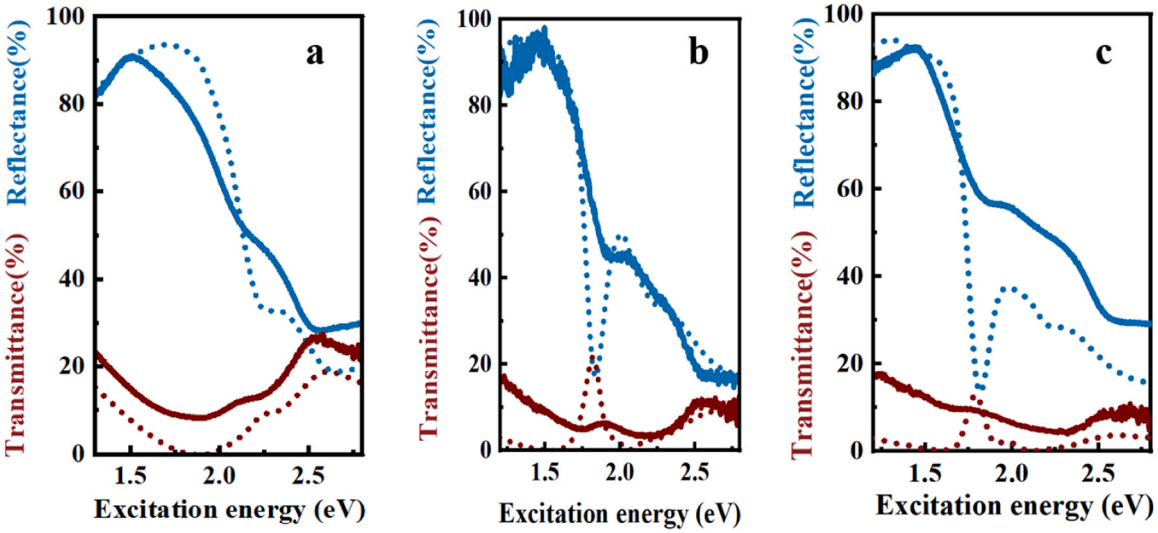

Fig. 3. Optical properties of AuNS@PS-SH monolayer superlattices. Experimental (solid line) and simulated (dashed line) reflection spectra (blue) and transmission spectra (red) of the (a) AuNS68@PS-SH, (b) AuNS91@PS-SH, and (c) AuNS114@PS-SH superlattice monolayers. The spectra highlight the size-dependent optical responses arising from LSPRs.

The intensity of Raman enhancement was evaluated by SERS enhancement factor (*EF*), which determined using the following equation [41]:

$$EF = \frac{I_s}{I_R}\frac{N_R}{N_s} \tag{2}$$

where I_S and I_R are the SERS intensities at 592 cm^{-1} of the sample and reference, while N_S and N_R are the concentrations of analyte molecules from the sample and reference, respectively. The EF values for superlattices assembled from AuNS68@PS-SH, AuNS91@PS-SH, and AuNS114@PS-SH are 1.3×10^2, 3.2×10^2, and 6.4×10^2, respectively. The results demonstrate that larger AuNSs (114 nm) generated significantly higher SERS enhancement due to more pronounced plasmonic coupling and increased density of hotspots between particles.

We investigated the signal reproducibility of superlattices by calculating the relative standard deviation (RSD) of the Raman peak intensity at 592 cm^{-1} for 100 sets of SERS signals (Figure S11). Results show that as AuNS size increases, the Raman intensity rises, with AuNS114@PS-SH (blue) showing the strongest signal but the highest RSD (19.6 %), indicating more fluctuation, The main sources include: (1) slight deviations in laser focusing position-although a microscopic objective was used for positioning, minor misalignments between the laser spot and the superlattice hotspot regions may cause variations in local signal intensity; (2) minor differences in hotspot density—the overall superlattice arrangement is uniform, but microscopic variations in particle spacing and packing may affect the distribution of electromagnetic hotspots; (3) the shielding effect of residual PS-SH ligands—some remaining ligands on the gold nanoparticle surfaces may partially hinder probe molecules from approaching the hotspot regions, leading to signal fluctuations. AuNS91@PS-SH (red) achieves

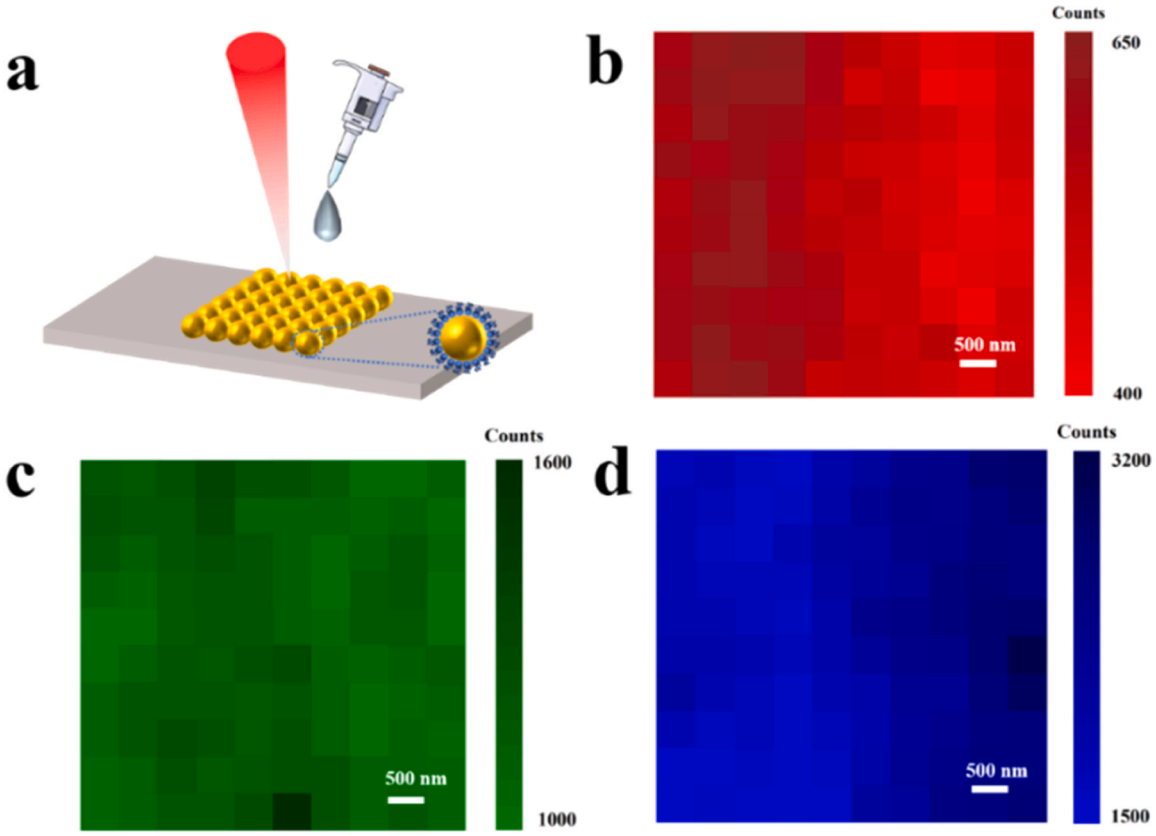

Fig. 4. (a) Schematic illustration of Raman test sample preparation diagram (b-d): Plotting of the Raman intensities at 592 cm^{-1} characteristic peaks of different superlattices: (b) AuNS68@PS-SH, (c) AuNS91@PS-SH, and (d) AuNS114@PS-SH.

the best balance of signal strength and stability (RSD 8.5 %), while AuNS68@PS-SH (gray) has the lowest signal but higher stability (RSD 13.4 %). This indicates that larger-sized AuNSs can enhance the SERS signal, but the uniformity decreases

The SERS activity is closely related to the local near-field enhancement of nanostructures. To investigate this relationship, we simulated the near-field distribution of the AuNS superlattice using the FDTD method (Fig. 5a). The computational model consisted of a periodic AuNSs array, with periodic boundary conditions, and the propagation direction is set perpendicular to the plane of superlattice. The simulated near-field distribution revealed that the local electromagnetic field enhancement was primarily in the gaps between AuNSs, confirming that hotspots were located at interparticle junctions. The near-field enhancement varied with the diameter of AuNSs. Specifically, for AuNSs with diameters of 68 nm, 91 nm, and 114 nm, the maximum $|E/E_0|$ values are 115, 131, and 169, respectively. The results indicate that the electromagnetic near-field enhancement was maximized at a particle diameter of 114 nm. This may be attributed to: 1. LSPR tuning. The LSPR of the 114 nm AuNS array was closest to the 633 nm laser excitation wavelength. 2. Gap-dependent field amplification. In the superlattice of larger gold nanospheres, smaller gaps between particles generated stronger localized electric fields, further amplifying the SERS effects. The trend observed in the theoretical simulations aligns well with the experimental SERS spectra results. As the nanoparticle diameter increased, the intensity of near-field hotspots between particles progressively enhanced. This intensified near-field enhancement significantly amplified the SERS effect, confirming the direct relationship between particle size, gap hotspots, and SERS activity.

We performed SERS detection of Nile red dye molecules at different concentrations and observed a prominent characteristic peak at 592 cm^{-1}, and additional low-intensity peaks at 674, 1157, 1496, and 1642 cm^{-1} [40]. As shown in Fig. 6a, the SERS enhancement factor, based on the lateral size of the plasmonic hotspots, was estimated to be between 10^2 and 10^4. The relationship between SERS intensity and concentration covered a concentration range spanning 5 orders of magnitude (Fig. 6a, b). The Raman intensity of the Nile Red peak at 591 cm^{-1} was fitted using the equation $Y = 1.85 \times x^{-5.7}$. This fit indicates that the superlattice fabricated by the current method exhibited an excellent relationship between SERS intensity and analyte concentration, demonstrating the high reliability of the SERS substrate.

In addition, the sensitivity of the AuNS superlattice enabled the detection of ultra-low analyte concentrations. For Nile red with a concentration of 10^{-9} M, although the overall signal intensity decreased (due to the reduction of adsorbed molecules on the superlattice surface), the SERS activity remained strong, achieving an intensity of 10^2, further confirming the high sensitivity of the superlattice as a SERS substrate.

The electric field strength in plasmonic nanogap is closely related to the excitation wavelength, and it has been reported that maximum SERS intensity occurs when the plasmonic resonance wavelength aligns between the excitation wavelength and the Raman emission wavelength of the analyte [42]. Therefore, to investigate the influence of excitation wavelengths on SERS performance, we conducted SERS measurements using excitation wavelengths of 532 nm, 633 nm, and 785 nm, to excite the AuNS superlattice (68 nm diameter, Fig. 6c). When the excitation wavelength is 633 nm, it resonates with the LSPR of the AuNS68@PS-SH superlattice, resulting in the strongest Raman signal and significant field enhancement effects. This resonance enhancement effect creates dense SERS hotspots between adjacent nanoparticles, and the local field enhancement promotes the interaction between molecules and surface plasmons, further improving SERS sensitivity and signal strength. Therefore, the 633 nm excitation wavelength shows the best enhancement effect in this study. In contrast, for the 532 nm and 785 nm excitation wavelengths, although they still excite the LSPR of the AuNS superlattice, the resonance effect with the LSPR is not perfectly matched,

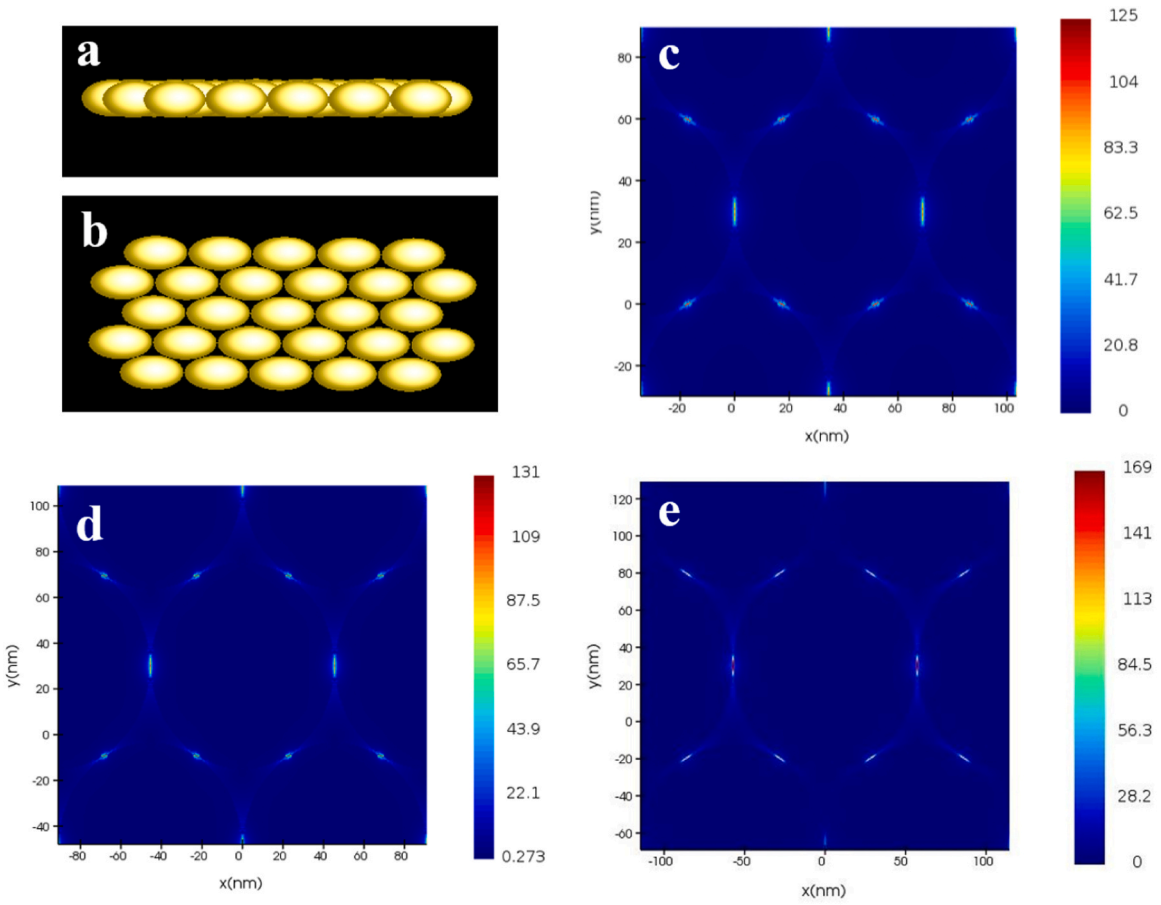

Fig. 5. The electric-field distribution obtained from FDTD simulations. (a,b) The computational model representing a reproducible unit of AuNS array with periodic boundary conditions: (a) side view and (b) top view. (c)-(e) Electromagnetic near-filed distributions of superlattices composed of AuNSs with different diameters: (c) 68 nm, (d) 91 nm, and (e) 114 nm. For AuNSs with diameters of 68 nm, 91 nm, and 114 nm, the maximum $|E/E_0|$ values are 115, 131, and 169, respectively. The results illustrate size-dependent hot-spot formation, with increased near-field enhancement observed for larger nanoparticles due to stronger plasmonic coupling.

leading to weaker SERS enhancement at these wavelengths. Specifically, the resonance between the 532 nm excitation wavelength and the LSPR of the AuNS superlattice is weak, resulting in a smaller surface field enhancement and a weaker Raman signal. Similarly, the 785 nm laser did not produce the same strong enhancement effect as the 633 nm laser, indicating that different excitation wavelengths have a significant impact on the field enhancement effect of the superlattice.

To better explain the experimental results, we used the finite-difference time-domain (FDTD) method to study the electric field distribution of the AuNS superlattice and analyze the effects of different excitation wavelengths and nanoparticle sizes on field enhancement. The simulated results (shown in Figs. S12-S14) reveal significant differences in the electric field distribution of the AuNS superlattice at excitation wavelengths of 532 nm, 633 nm, and 785 nm. Among these, at the 633 nm excitation wavelength, the local electromagnetic field enhancement is most pronounced, with the field intensity concentrated in the gap region between the nanoparticles, forming a strong "hotspot" effect. This result is consistent with the trend observed in the experimental SERS signal, where the SERS signal intensity reaches its maximum at 633 nm excitation.

To further demonstrate the universality of the superlattice, we performed SERS detection of methylene blue (MB, 10^{-8} M) on the AuNS@68 nm superlattice. The SERS detection was conducted using a 633 nm laser wavelength, a power of 1 %, an exposure time of 1 s, and a single accumulation. The MB characteristic peak at 1621 cm^{-1} was easily detected. There is no significant difference in the uniformity of the superlattice mapping image, and AuNSs superlattices exhibit very uniform Raman response (Fig. 6d). The SERS enhancement for MB exceeded 10^3, indicating that the superlattice substrate is highly effective across multiple analytes, not limited to Nile Red. This universality highlights that the nanostructure provides strong SERS enhancement for a wide range of molecules, and broad applicable in fields such as chemical sensing, biological detection, SERS-based diagnostics [43,44].

3. Conclusions

In summary, we successfully synthesized large and uniform gold nanospheres and assembled superlattices with precise size control to tailor their optical and SERS properties. The study showed that as the nanoparticle size increased, light–matter coupling was enhanced, leading to a gradual redshift of reflection dips and transmission peaks. Both experimental measurements and FDTD simulations demonstrated that superlattices composed of larger gold nanospheres, especially under 633 nm excitation, exhibited stronger localized electromagnetic fields, significantly improving SERS performance. Moreover, these superlattices maintained excellent sensitivity even under low analyte concentrations and low laser power conditions, highlighting their advantages as efficient SERS substrates. The successful detection of Nile Red and methylene blue further confirmed the broad applicability of these superlattices in chemical sensing. With high sensitivity, reproducibility, and uniformity, these superlattices serve as powerful platforms for SERS-based chemical and biological sensing, opening new avenues for advanced detection technologies and nanophotonic applications.

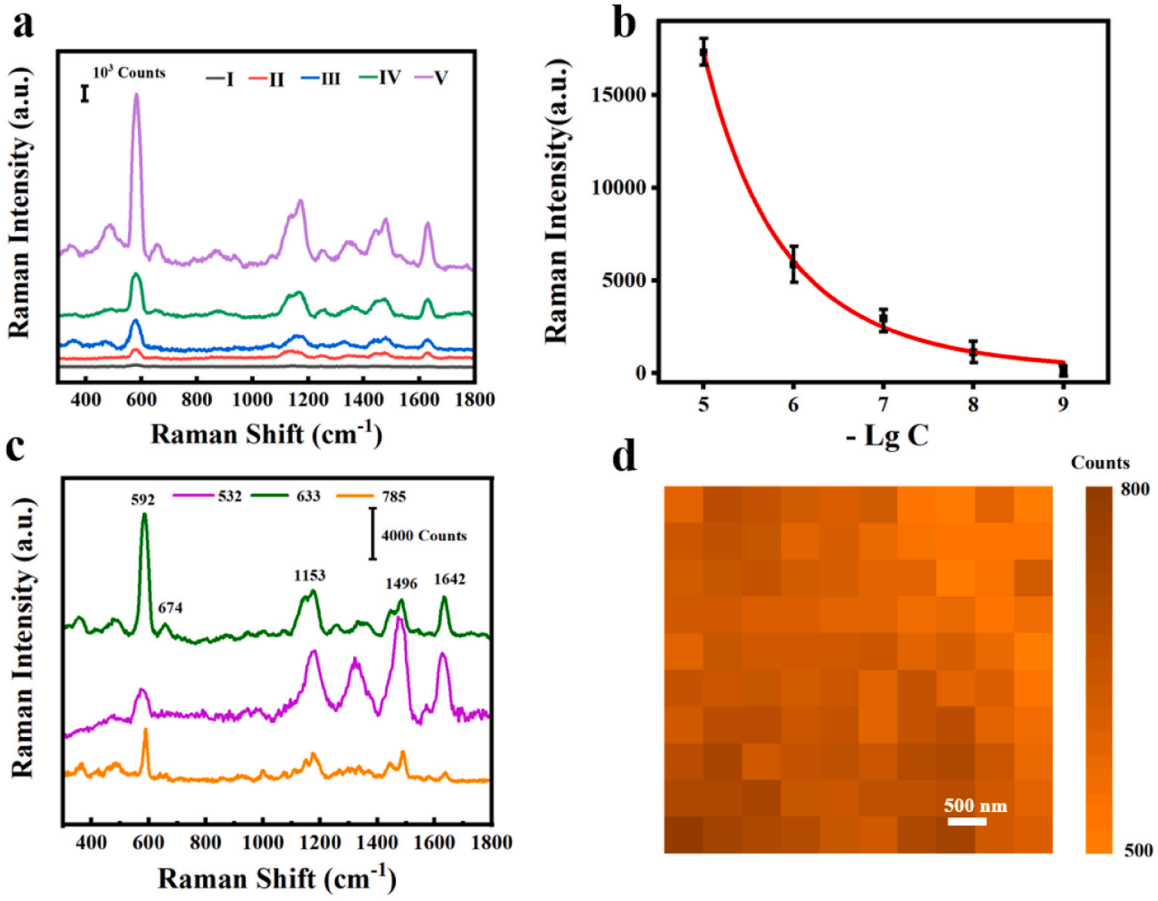

Fig. 6. (a) Raman spectra obtained using AuNS68@PS-SH superlattice for the detection of Nile red at concentrations of 10^{-5} M to 10^{-9} M (I) 10^{-9} M; (II) 10^{-8} M; (III) 10^{-7} M; (IV) 10^{-6} M; (V) 10^{-5} M. (b) The relationship between Nile red concentration and the Raman intensity at 592 cm^{-1}. The error bars were obtained based on 5 Raman spectra. (c) Raman spectra of AuNS68@PS-SH superlattice with Nile red molecules under excitation at laser wavelengths (532 nm, 633 nm, 785 nm). (d) Raman spectra of methylene blue, highlighting the characteristic peak at 1621 cm^{-1}.

4. Experimental section

4.1. Materials

All chemicals were obtained from commercial suppliers and used without further purification. Hexadecyltrimethylammonium bromide (CTAB, >99.0 %) was purchased from TCI America. Chloroauric acid ($HAuCl_4$), L-ascorbic acid (AA, >99.99 %), cetyltrimethylammonium chloride (CTAC, 99 %), Nile red, methylene blue (MB), methanol (99.5 %) were purchased from Shanghai Macklin Biochemical Technology Co. Ltd. Diethylene glycol (DEG, >98.0 %), sodium borohydride ($NaBH_4$,>98 %), and tetrahydrofuran (THF, 99.0 %) were purchased from Shanghai Aladdin Biochemical Technology Co., Ltd. Thiol-terminated polystyrene (PS-SH, average M_n = 11,000, PDI ≤ 1.1) was purchased form MKCH2403. Toluene (TOL, ≥99.5 %) was purchased from National Pharmaceutical Group Chemical Reagent Co., Ltd. Ultrapure water (>18.2 MΩ) obtained from a Milli-Q water system was used in all experiments. All glassware were cleaned using freshly prepared aqua regia (HCl:HNO_3 in a 3:1 ratio by volume) followed by rinsing with copious amounts of ultrapure water to ensure the removal of any contaminants.

4.2. Synthesis of the AuNSs

The AuNS samples were prepared using the seed-mediated growth method [15]. Firstly, under vigorous stirring, a freshly prepared ice cold $NaBH_4$ (10 mM, 0.60 mL) solution was added to a mixed solution of $HAuCl_4$ (10 mM, 0.25 mL) and CTAB (100 mM, 9.75 mL). The mixture was slowly stirred at room temperature (160 rpm) for 3 h. CTAB (100 mM, 9.75 mL), water (190 mL), $HAuCl_4$ (10 mM, 4 mL), and AA (0.1 M, 15 mL) were sequentially added to a 500 mL flask to prepare a growth solution. Subsequently, 0.12 mL of the prepared seed solution was injected into the growth solution, and the reaction mixture was gently shaken and allowed to stand overnight at room temperature. The resulting small gold nanospheres were washed, concentrated, and dispersed in water. The washing process helps remove excess surfactant and unreacted precursors. Finally, the extinction intensity of the plasmon peak was adjusted to 1.52 in a 10 mm optical path colorimetric dish.

Next, small AuNSs with volumes of 0.5 mL, 0.2 mL, and 0.1 mL were added to CTAC solution (25 mM, 30 mL). For small gold nanospheres with a volume of 0.2 mL or less, the solution was diluted four times with water before use. After sequentially adding AA (0.1 M, 0.75 mL) and $HAuCl_4$ (10 mM, 1.5 mL), the mixed solution was stirred at 160 rpm for 2 h in a 45 ℃ water bath to obtain gold nanopolyhedron, which were then dispersed in CTAB solution (20 mM, 30 mL). Finally, $HAuCl_4$ (10 mM, 0.2 mL) was added to the gold nanopolyhedron solution and stirred at 160 rpm for 2 h in a 45 ℃ water bath to obtain the AuNS samples.

All absorption measurements were captured on a UV-1900i spectrophotometer (SHIMADZU, Japan) with a light path of 10.0 mm, using a glass colorimetric tube filled with Milli-Q water or toluene as the reference. Transmission electron microscopy (TEM) images were acquired using an HT-7700 microscope (HITACHI, Japan) operated at 100.0 kV.

4.3. Surface modification of AuNSs

In a typical procedure, a 10 mL solution of AuNS@CTAB was centrifuged twice to remove excess CTAB. After the second centrifugation, the concentrated solution volume was reduced to < 100 μL. This concentrated solution was then added to a 2 mL THF solution containing PS-SH polymer ligands (M_n = 11,000, 2.5 mg). The mixture was subjected to 2 h of sonication to facilitate interaction between AuNSs and PS-SH [23]. Sonication helps overcome steric barriers, promoting efficient ligand exchange. After sonication, the mixture was allowed to stand for 24 h. The AuNS@PS-SH were then dispersed in THF, and the supernatant was removed by centrifugation (9000 rpm, 10 min) to obtain purified PS-tethered AuNSs. The AuNS@PS-SH were washed with ethanol, followed by centrifugation (9000 rpm, 10 min), and then dispersed in toluene. This washing step with toluene ensures complete separation of AuNS@PS-SH from residual CTAB surfactants and free PS-SH. The AuNS@PS-SH were redispersed in 10 mL of toluene.

4.4. Self-assembly of AuNS@PS-SH superlattices

AuNS@PS-SH self-assembled to form a monolayer superlattice at the liquid -liquid interface. Initially, 1.5 mL of toluene containing AuNS@PS-SH was centrifuged to reduce the volume to < 100 μL. The concentration step increases particle density, promoting uniform monolayer formation. The concentrated solution was then pipetted onto a polytetrafluoroethylene (PTFE) trough (side length ~ 1.5 cm) containing 700 μL of diethylene glycol (DEG) as the subphase. A glass coverslip was placed over the trough to allow slow evaporation of toluene. After waiting for at least 12 h, as toluene evaporated and system entropy maximized, a monolayer of gold nanoparticles formed at the DEG subphase surface. The film was transferred onto a quartz or silicon substrate and dried in an oven at 80 ℃. Transmission electron microscopy (TEM) images were acquired using an HT-7700 microscope (HITACHI, Japan) operated at 100.0 kV. Scanning electron microscopy (SEM) images were obtained using a Gemini SEM 300 (Zeiss, Germany) operating at 3.0 kV.

4.5. Optical microscopy

Optical microscopy was conducted using an Olympus BX53 optical microscope, paired with a halogen lamp (100 W) and a NOVA 2S-EX spectrometer. Using an objective lens with a numerical aperture (NA) of 0.80 and a magnification of 100x, white light excitation and collection of scattered and transmitted light were performed on the AuNS superlattices. The scattered light and transmitted light were directed towards the entrance slit of the monochromator. By subtracting the background spectra of adjacent particle-free regions, the scattering and transmission spectra of the superlattices were obtained. To normalize the data, the collected spectra were divided by the pre-calibrated response curve of the entire optical system.

4.6. SERS measurements

SERS measurements were performed using a Raman spectrometer (LabRAM HREvolution, HORIBA) equipped with a 100x objective lens. The samples were excited using laser sources with wavelengths of 532 nm, 633 nm, and 785 nm. Silicon wafers were used as the substrates. Before depositing the superlattices, the wafers were ultrasonically cleaned in acetone water for 5 min, rinsed twice with ethanol, and subsequently dried. Then, the superlattices were transferred onto the silicon wafer substrate. Next, 10 μL of Nile red or methylene blue solution of different concentrations was drop-cast onto the superlattices and dried again. Using the 100x objective lens, the laser spot size was approximately 1 μm. Under 1 % neutral density filters, the laser powers for 532 nm and 633 nm were 34 μW and 26 μW, respectively; for the 785 nm laser, a 5 % filter was used, yielding a power of approximately 175 μW. The integration time was set to 1 s per measurement. For Raman mapping, the 633 nm laser was used with 1 % power, a 1-second integration time, a scanning area of 5 μm x 5 μm, and a step size of 500 nm.

4.7. FDTD simulations

Finite Difference Time Domain (FDTD) simulations were performed using FDTD Solutions 8.0 software developed by Lumerical Solutions Inc. In all simulations, the dielectric constant of AuNSs was taken from Johnson and Christy [45], and polystyrene ligand molecules were simulated as a dielectric material with a refractive index of $n = 1.4$, filling the gaps between AuNSs. The size of the nanoparticles was determined based on the statistical results of the average size measured from the experimental results. The diameters of the AuNSs were set to 68 nm, 91 nm, and 114 nm, respectively. For the optical response simulations, 68 nm AuNSs were arranged in a hexagonal lattice with a 3 nm interparticle gap, while 91 nm and 114 nm AuNSs were arranged in a hexagonal lattice with a 1 nm interparticle gap. These configurations were used for all AuNS superlattice calculations.

The simulation domain for the superlattice was defined as a single unit cell, using periodic boundary conditions in the x and y directions, use a perfect matching layer (PML) in the z direction. The light was injected from a plane wave source along the z direction. Transmittance and reflectance were recorded by power monitors positioned behind the nanoparticle layer and the light source. The mesh size of all samples was set to 0.5 nm.

To calculate the electric field distribution of the periodic AuNSs superlattices, the wavelengths of the light sources were set to 532 nm, 633 nm, and 785 nm. Based on the average size statistical results measured from the experiments, the interparticle distances for the 68 nm, 91 nm, and 114 nm nanoparticles are set to 3 nm, 1 nm, and 0.5 nm, respectively. Periodic boundary conditions were applied in the y-axis direction, while PML boundaries were used in the z- direction, The mesh size for these calculations was consistently set to 0.5 nm.

CRediT authorship contribution statement

Yiqiang Gao: Writing – review & editing, Supervision, Investigation. **Tian-Song Deng:** Writing – review & editing, Supervision, Investigation, Funding acquisition, Conceptualization. **Gui-Lin Wu:** Methodology, Investigation, Data curation. **Kun-Peng Wang:** Methodology, Investigation, Data curation. **Jia-Fei Gao:** Writing – review & editing, Writing – original draft, Methodology, Investigation, Data curation. **Jie Liu:** Writing – review & editing, Visualization, Supervision.

Declaration of Competing Interest

The authors declare that they have no known competing financial interests or personal relationships that could have appeared to influence the work reported in this paper.

Acknowledgements

The authors thank Sudan Shen for her assistance in TEM at State Key Laboratory of Chemical Engineering (Zhejiang University). T. S. Deng acknowledge financial support from Zhejiang Provincial Natural Science Foundation (Grant: LY24F050008) and National Natural Science Foundation of China (NSFC, Grant: 61905056).

Appendix A. Supporting information

Supplementary data associated with this article can be found in the online version at doi:10.1016/j.colsurfa.2025.137761.

Data Availability

Data will be made available on request.

References

[1] S.J. Barrow, X. Wei, J.S. Baldauf, A.M. Funston, P. Mulvaney, The surface plasmon modes of self-assembled gold nanocrystals, Nat. Commun. 3 (2012) 1275, https://doi.org/10.1038/ncomms2289.

[2] N.S. Mueller, Y. Okamura, B.G.M. Vieira, S. Juergensen, H. Lange, E.B. Barros, F. Schulz, S. Reich, Deep strong light-matter coupling in plasmonic nanoparticle crystals, Nature 583 (2020) 780–784, https://doi.org/10.1038/s41586-020-2508-1.

[3] Y.H. Lee, W. Shi, H.K. Lee, R. Jiang, I.Y. Phang, Y. Cui, L. Isa, Y. Yang, J. Wang, S. Li, X.Y. Ling, Nanoscale surface chemistry directs the tunable assembly of silver octahedra into three two-dimensional plasmonic superlattices, Nat. Commun. 6 (2015) 6990, https://doi.org/10.1038/ncomms7990.

[4] J. Cambiasso, M. KoNig, E. Cortes, S. SchluCker, S.A. Maier, Surface-enhanced spectroscopies of a molecular monolayer in an all-dielectric nanoantenna, ACS Photonics 5 (2018) 1546–1557, https://doi.org/10.1021/acsphotonics.7b01604.

[5] W. Wei, Y. Wang, J. Ji, S. Zuo, W. Li, F. Bai, H. Fan, Fabrication of large-area arrays of vertically aligned gold nanorods, Nano Lett. 18 (2018) 4467–4472, https://doi.org/10.1021/acs.nanolett.8b01584.

[6] M.U. Amin, J.X. Fang, Self-assembled gold nano-bipyramids for solution-based surface-enhanced Raman spectroscopy detection, ACS Appl. Nano Mater. 5 (2022) 10421–10430, https://doi.org/10.1021/acsanm.2c01779.

[7] X. Chen, A. Cui, M. He, M. Yan, X. Zhang, J. Ruan, S. Yang, Slippery Au nanosphere monolayers with analyte enrichment and SERS enhancement functions, Nano Lett. 23 (2023) 6736–6743, https://doi.org/10.1021/acs.nanolett.3c02238.

[8] W. Ding, Y. Xia, H. Song, T. Li, D. Yang, A. Dong, Macroscopic superlattice membranes self-assembled from gold nanobipyramids with precisely tunable tip arrangements for SERS, Angew. Chem. 136 (2024) e202401945, https://doi.org/10.1002/anie.202401945.

[9] E.V. Shevchenko, M. Ringler, A. Schwemer, D.V. Talapin, T.A. Klar, A.L. Rogach, J. Feldmann, A.P. Alivisatos, Self-assembled binary superlattices of CdSe and Au nanocrystals and their fluorescence properties, J. Am. Chem. Soc. 130 (2008) 3274–3275, https://doi.org/10.1021/ja710619s.

[10] X. Ye, C. Zhu, P. Ercius, S.N. Raja, B. He, M.R. Jones, M.R. Hauwiller, Y. Liu, T. Xu, A.P. Alivisatos, Structural diversity in binary superlattices self-assembled from polymer-grafted nanocrystals, Nat. Commun. 6 (2015) 10052, https://doi.org/10.1038/ncomms10052.

[11] T. Udayabhaskararao, T. Altantzis, L. Houben, M. Coronado-Puchau, J. Langer, R. Popovitz-Biro, L.M. Liz-Marzán, L. Vuković, P. Král, S. Bals, Tunable porous nanoallotropes prepared by post-assembly etching of binary nanoparticle superlattices, Science 358 (2017) 514–518, https://doi.org/10.1126/science.aan6046.

[12] N.S. Mueller, B.G. Vieira, F. Schulz, P. Kusch, V. Oddone, E.B. Barros, H. Lange, S. Reich, Dark interlayer plasmons in colloidal gold nanoparticle Bi-and few-layers, ACS Photonics 5 (2018) 3962–3969, https://doi.org/10.1021/acsphotonics.8b00898.

[13] H.Q. Liu, J.Y. Zeng, L.P. Song, L.L. Zhang, Z.H. Chen, J.H. Li, Z.D. Xiao, F.M. Su, Y. J. Huang, Etched-spiky Au@Ag plasmonic-superstructure monolayer films for triple amplification of surface-enhanced Raman scattering signals, Nanoscale Horiz. 7 (2022) 554–561, https://doi.org/10.1039/d2nh00023g.

[14] Y.-J. Lee, N.B. Schade, L. Sun, J.A. Fan, D.R. Bae, M.M. Mariscal, G. Lee, F. Capasso, S. Sacanna, V.N. Manoharan, Ultrasmooth, highly spherical monocrystalline gold particles for precision plasmonics, ACS Nano 7 (2013) 11064–11070, https://doi.org/10.1021/nn404765w.

[15] Q.F. Ruan, L. Shao, Y.W. Shu, J.F. Wang, H.K. Wu, Growth of monodisperse gold nanospheres with diameters from 20 nm to 220 nm and their core/satellite nanostructures, Adv. Opt. Mater. 2 (2014) 65–73, https://doi.org/10.1002/adom.201300359.

[16] Y.Y. Cai, Y.C. Choi, C.R. Kagan, Chemical and physical properties of photonic noble-metal nanomaterials, Adv. Mater. 35 (2023) 2108104, https://doi.org/10.1002/adma.202108104.

[17] S. Lin, H.Y. Guan, Y.Q. Liu, S.N. Huang, J.M. Li, W.J. Hasi, Y.Z. Xu, J.X. Zou, B. Dong, Binary plasmonic assembly films with hotspot-type-dependent surface-enhanced Raman scattering properties, ACS Appl. Mater. Interfaces 13 (2021) 53289–53299, https://doi.org/10.1021/acsami.1c18565.

[18] G.Q. Fang, X. Lin, J.L. Wu, W. Xu, W. Hasi, B. Dong, Porous nanoframe based plasmonic structure with high-density hotspots for the quantitative detection of gaseous benzaldehyde, Small 21 (2025) 11, https://doi.org/10.1002/smll.202408670.

[19] X.N. Lin, F.C. Lei, X. Liang, Y. Jiao, X.F. Zhao, Z. Li, C. Zhang, J. Yu, Quantitative detection of trace nanoplastics (down to 50 nm) via surface-enhanced raman scattering based on the multiplex-feature coffee ring, OptoElectron. Adv. 14 (2025), https://doi.org/10.29026/oea.2025.240260.

[20] H. Yockell-Lelièvre, J. Desbiens, A.M. Ritcey, Two-dimensional self-organization of polystyrene-capped gold nanoparticles, Langmuir 23 (2007) 2843–2850, https://doi.org/10.1021/la062886b.

[21] M.A. Boles, M. Engel, D.V. Talapin, Self-assembly of colloidal nanocrystals: from intricate structures to functional materials, Chem. Rev. 116 (2016) 11220–11289, https://doi.org/10.1021/acs.chemrev.6b00196.

[22] K.J. Si, Y. Chen, Q. Shi, W. Cheng, Nanoparticle superlattices: the roles of soft ligands, Adv. Sci. 5 (2018) 1700179, https://doi.org/10.1002/advs.201700179.

[23] F. Schulz, O. Pavelka, F. Lehmkühler, F. Westermeier, Y. Okamura, N.S. Mueller, S. Reich, H. Lange, Structural order in plasmonic superlattices, Nat. Commun. 11 (2020) 3821, https://doi.org/10.1038/s41467-020-17632-4.

[24] F. Schulz, F. Westermeier, F. Dallari, V. Markmann, H. Lange, G. Grübel, F. Lehmkühler, Plasmonic supercrystals with a layered structure studied by a combined TEM-SAXS-XCCA approach, Adv. Mater. Interfaces 7 (2020) 2000919, https://doi.org/10.1002/admi.202000919.

[25] B.Gm Vieira, N.S. Mueller, E.B. Barros, S. Reich, Plasmonic properties of close-packed metallic nanoparticle mono-and bilayers, J. Phys. Chem. C 123 (2019) 17951–17960, https://doi.org/10.1021/acs.jpcc.9b03859.

[26] N.S. Mueller, B.G.M. Vieira, D. Hoeing, F. Schulz, E.B. Barros, H. Lange, S. Reich, Direct optical excitation of dark plasmons for hot electron generation, Faraday Discuss. 214 (2019) 159–173, https://doi.org/10.1039/c8fd00149a.

[27] D.S. Dong, R.F. Fu, Q.Q. Shi, W.L. Cheng, Self-assembly and characterization of 2D plasmene nanosheets, Nat. Protoc. 14 (2019) 2691–2706, https://doi.org/10.1038/s41596-019-0200-4.

[28] X. Lin, G.Q. Fang, Y.L. Liu, Y.Y. He, L. Wang, B. Dong, Marangoni effect-driven transfer and compression at three-phase interfaces for highly reproducible nanoparticle monolayers, J. Phys. Chem. Lett. 11 (2020) 3573–3581, https://doi.org/10.1021/acs.jpclett.0c01116.

[29] L.P. Song, B.X. Ben, Q. Cheng, X.Y. Wang, X.N. Luo, X. Chen, T. Chen, Y.J. Huang, Instant interfacial self-assembly for homogeneous nanoparticle monolayer enabled conformal "lift-on" thin film technology, Sci. Adv. 7 (2021) 9, https://doi.org/10.1126/sciadv.abk2852.

[30] M. Baia, L. Baia, S. Astilean, Gold nanostructured films deposited on polystyrene colloidal crystal templates for surface-enhanced Raman spectroscopy, Chem. Phys. Lett. 404 (2005) 3–8, https://doi.org/10.1016/j.cplett.2005.01.052.

[31] V.A. Khanadeev, B.N. Khlebtsov, S.A. Klimova, M.Y. Tsvetkov, V.N. Bagratashvili, G.B. Sukhorukov, N.G. Khlebtsov, Large-scale high-quality 2D silica crystals: dip-drawing formation and decoration with gold nanorods and nanospheres for SERS analysis, Nanotechnology 25 (2014), https://doi.org/10.1088/0957-4484/25/40/405602.

[32] Z.V. Saponjic, R. Csencsits, T. Rajh, N.M. Dimitrijevic, Self-assembly of TOPO-derivatized silver nanoparticles into multilayered film, Chem. Mater. 15 (2003) 4521–4526, https://doi.org/10.1021/cm030381q.

[33] A. Dong, J. Chen, P.M. Vora, J.M. Kikkawa, C.B. Murray, Binary nanocrystal superlattice membranes self-assembled at the liquid–air interface, Nature 466 (2010) 474–477, https://doi.org/10.1038/nature09188.

[34] N.S. Mueller, E. Pfitzner, Y. Okamura, G. Gordeev, P. Kusch, H. Lange, J. Heberle, F. Schulz, S. Reich, Surface-enhanced Raman scattering and surface-enhanced infrared absorption by plasmon polaritons in three-dimensional nanoparticle supercrystals, ACS Nano 15 (2021) 5523–5533, https://doi.org/10.1021/acsnano.1c00352.

[35] A. Pinchuk, G.Von Plessen, U. Kreibig, Influence of interband electronic transitions on the optical absorption in metallic nanoparticles, J. Phys. D Appl. Phys. 37 (2004) 3133, https://doi.org/10.1088/0022-3727/37/22/012.

[36] H. Yockell-Lelièvre, F. Lussier, J.-F. Masson, Influence of the particle shape and density of self-assembled gold nanoparticle sensors on LSPR and SERS, J. Phys. Chem. C 119 (2015) 28577–28585, https://doi.org/10.1021/acs.jpcc.5b09570.

[37] X. Lin, S. Lin, Y. Liu, H. Zhao, L. Wang, W. Hasi, Self-assembly of large-scale two-dimensional plasmonic superlattices based on single-crystal Au nanospheres and the FDTD simulation of its optical properties, Plasmonics 13 (2018) 1749–1758, https://doi.org/10.1007/s11468-017-0688-9.

[38] S.E.J. Bell, G. Charron, E. Cortes, J. Kneipp, M.L. De La Chapelle, J. Langer, M. Prochazka, V. Tran, Towards reliable and quantitative surface-enhanced raman scattering (SERS): from key parameters to good analytical practice, Angew. Chem. Int. Ed. 59 (2020) 5454–5462, https://doi.org/10.1002/anie.201908154.

[39] X. Li, D. Zhang, L. Wang, L. Yin, X. Qi, M. Zou, Q. Chen, Z. Yu, P. Liang, Shrinking gap between nanoparticles in gold nanofilms to enhance surface-enhanced Raman spectroscopy performance investigated by both experimental and theoretical methods, Appl. Surf. Sci. 638 (2023) 157823, https://doi.org/10.1016/j.apsusc.2023.157823.

[40] A. Ramya, P. Ambily, B. Sujitha, M. Arumugam, K.K. Maiti, Single cell lipid profiling of Scenedesmus quadricauda CASA-CC202 under nitrogen starved condition by surface enhanced Raman scattering (SERS) fingerprinting, Algal Res. 25 (2017) 200–206, https://doi.org/10.1016/j.algal.2017.05.011.

[41] J.E.S. Van Der Hoeven, H. Gurunarayanan, M. Bransen, P.E. D.a.M. De Winter, A. De Jongh, Van Blaaderen, Silica-coated gold nanorod supraparticles: a tunable platform for surface enhanced Raman spectroscopy, Adv. Funct. Mater. 32 (2022) 2200148, https://doi.org/10.1002/adfm.202200148.

[42] C.J. Addison, A.G. Brolo, Nanoparticle-containing structures as a substrate for surface-enhanced Raman scattering, Langmuir 22 (2006) 8696–8702, https://doi.org/10.1021/la061598c.

[43] C. Matricardi, C. Hanske, J.L. Garcia-Pomar, J. Langer, A. Mihi, L.M. Liz-Marzán, Gold nanoparticle plasmonic superlattices as surface-enhanced Raman spectroscopy substrates, ACS Nano 12 (2018) 8531–8539, https://doi.org/10.1021/acsnano.8b04073.

[44] J. Langer, D. Jimenez De Aberasturi, J. Aizpurua, R.A. Alvarez-Puebla, B. Auguié, J.J. Baumberg, G.C. Bazan, S.E. Bell, A. Boisen, A.G. Brolo, Present and future of surface-enhanced Raman scattering, ACS Nano 14 (2019) 28–117, https://doi.org/10.1021/acsnano.9b04224.

[45] P.B. Johnson, R.-W. Christy, Optical constants of the noble metals, Phys. Rev. B 6 (1972) 4370, https://doi.org/10.1103/PhysRevB.6.4370.

Supporting Information

Size-tunable gold nanosphere superlattices with enhanced SERS performance

Jia-Fei Gao[1], Jie Liu[1,], Gui-Lin Wu[1], Kun-Peng Wang[1], Yiqiang Gao[1,*], and Tian-Song Deng[1,2,*]*

[1]School of Electronics and Information Engineering, Hangzhou Dianzi University, Hangzhou 310018, China

[2]Key Laboratory of Micro-nano Sensing and IoT of Wenzhou, Wenzhou Institute of Hangzhou Dianzi University, Wenzhou, 325038, China

[*]Corresponding author. E-mail: liujie4209@hdu.edu.cn, yqgao@hdu.edu.cn, dengts@pku.edu.cn

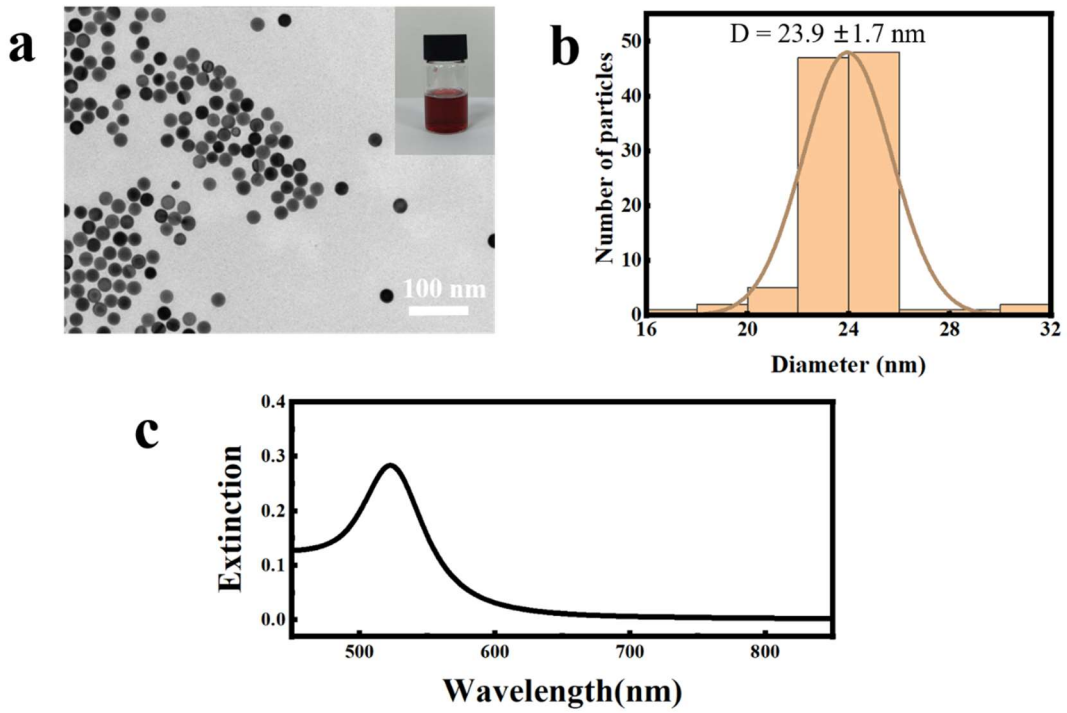

Figure S1. (a) SEM images of the small gold nanospheres (AuNSs) with diameters of 24 nm. Inset: Corresponding image of the small AuNSs colloidal solution. (b) Particle size distribution of small AuNSs conforms to a fitted Gaussian distribution curve. (c) Extinction spectrum of the small AuNSs.

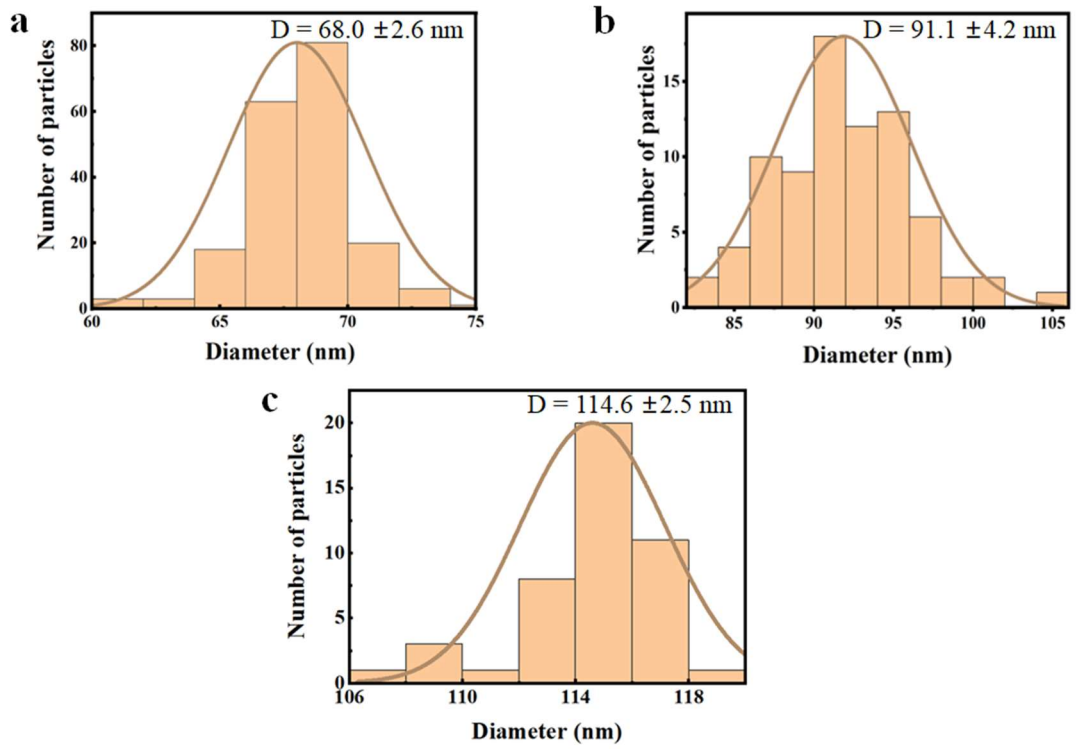

Figure S2. Particle size distribution map of AuNSs with different diameters. (a) 68.0±2.6 nm, (b) 91.1±4.2 nm, and (c) 114.6±2.5 nm.

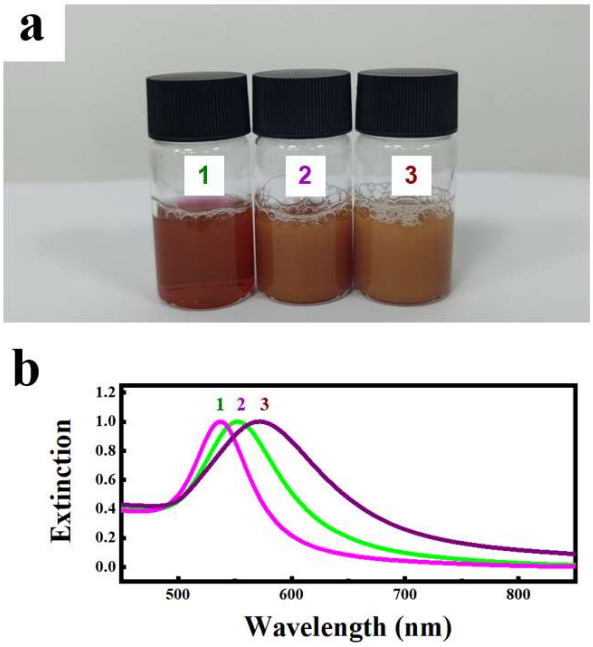

Figure S3. Digital photographs and extinction spectra of the AuNS samples. (a) Digital photograph of colloidal AuNS solutions of with different sizes, arranged from left to right corresponding to samples 1, 2, and 3, respectively. (b) Normalized extinction spectra of samples 1, 2, and 3 measured using a UV/visible/NIR spectrophotometer. The spectra show distinct size-dependent plasmonic peaks due to variations in nanoparticle diameter. Samples 1, 2, and 3 correspond to AuNSs with average diameters of 68.0 ± 2.6 nm, 91.1 ± 4.2 nm, and 114.6 ± 2.5 nm, respectively. In the FDTD simulations, AuNSs were modeled using the corresponding average diameters. All of the extinction spectra are normalized for comparative purpose.

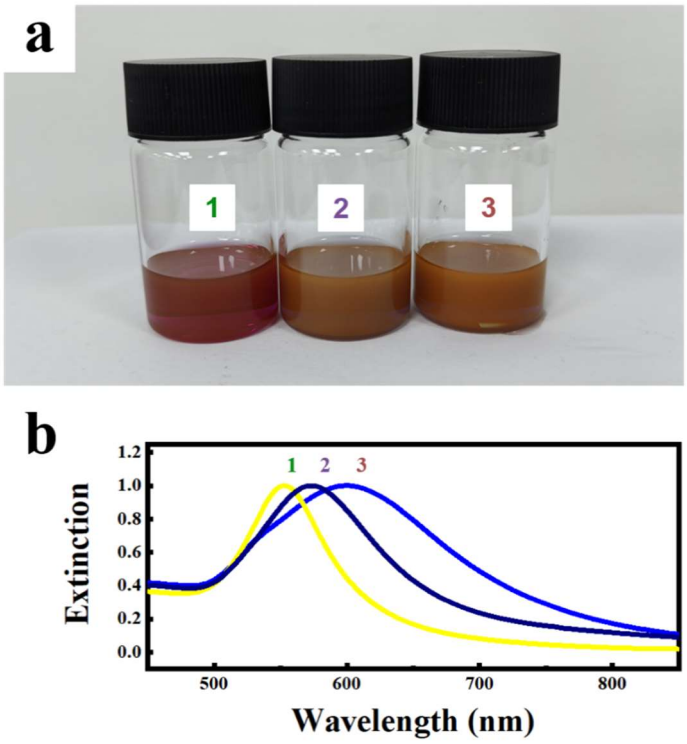

Figure S4. Digital photographs and extinction spectra of the Au-NS@PS-SH samples in toluene. (a) Digital photographs of Au-NS@PS-SH colloidal solutions with different nanoparticle sizes. (b) Normalized extinction spectra of samples 1, 2, and 3 measured using a UV/visible/NIR spectrophotometer. Samples 1, 2 and 3 correspond to Au-NS@PS-SH with average diameters the same as AuNSs shown in Figure S3. For comparison, all extinction spectra were normalized.

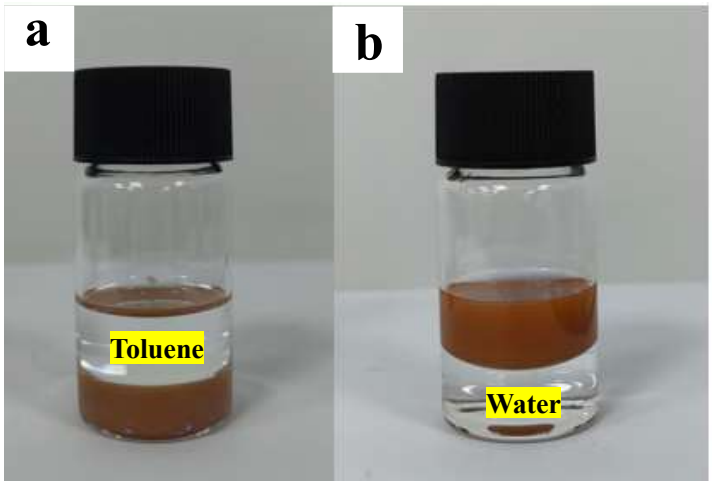

Figure S5. a, b) Phase transfer of AuNSs from water (lower phase) to toluene (upper phase). The glass bottles on the left and right show the same samples before and after phase transfer. The successful phase transfer is evidenced by the color change of the upper phase, indicating ligand exchange from CTAB to PS-SH.

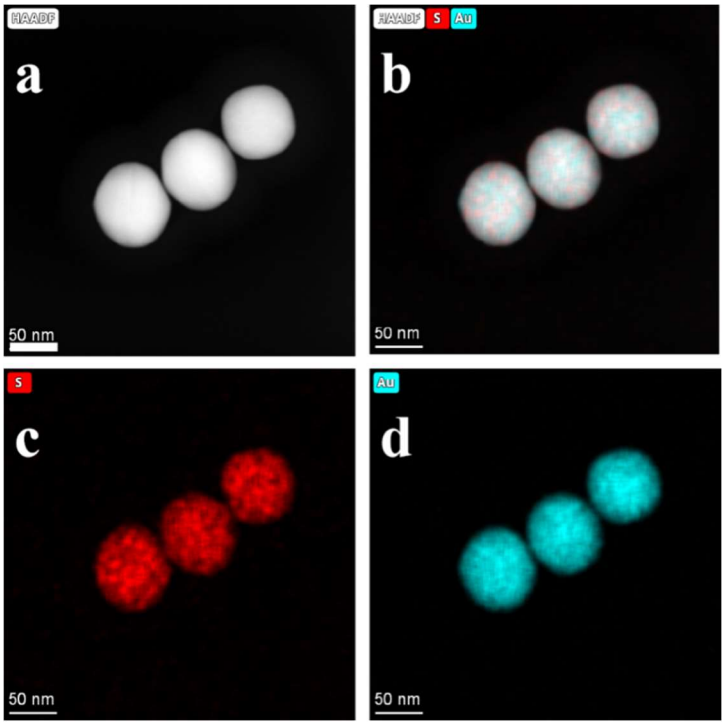

Figure S6. Characterization of modified AuNSs: (a) HADDF-STEM image; elemental analysis (b, c, d) Au (blue), S (red).

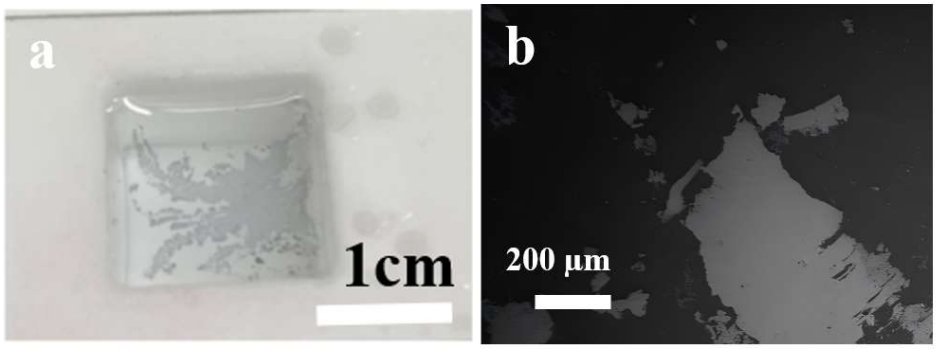

Figure S7. Physical photos and low-magnification scanning electron microscopy (SEM) images of the monolayer film.

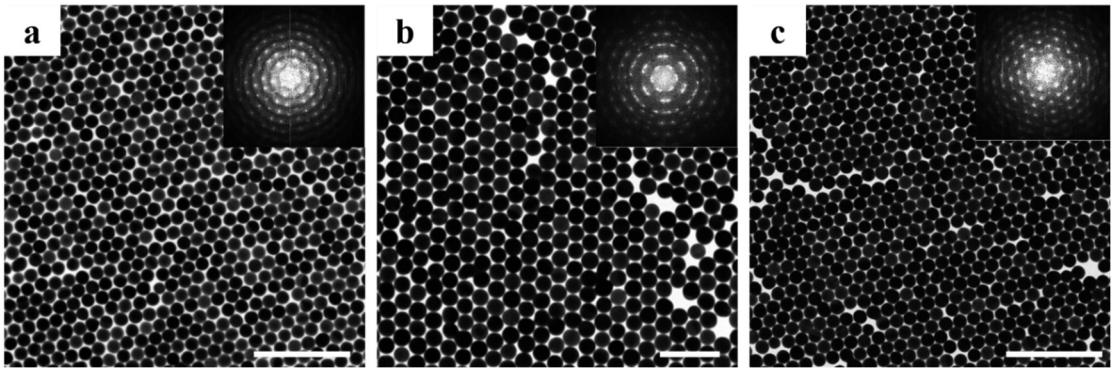

Figure S8. TEM images of monolayer superlattice samples formed by gold nanospheres of different sizes (a) 68.0 ± 2.6 nm. (b) 91.1 ± 4.2 nm. (c) 114.6 ± 2.5 nm. The inset shows the FFT of the digital image. TEM scalebar: (a, c) 500 nm; (b) 200 nm.

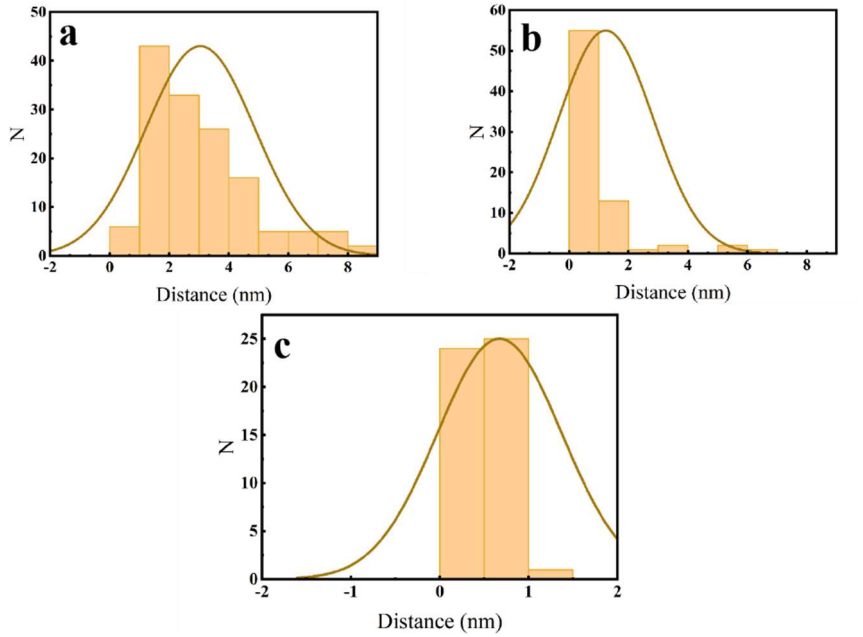

Figure S9. Interparticle spacing distribution of self-assembled superlattices of AuNSs with different sizes: (a) 68 nm, (b) 91 nm, (c) 114 nm.

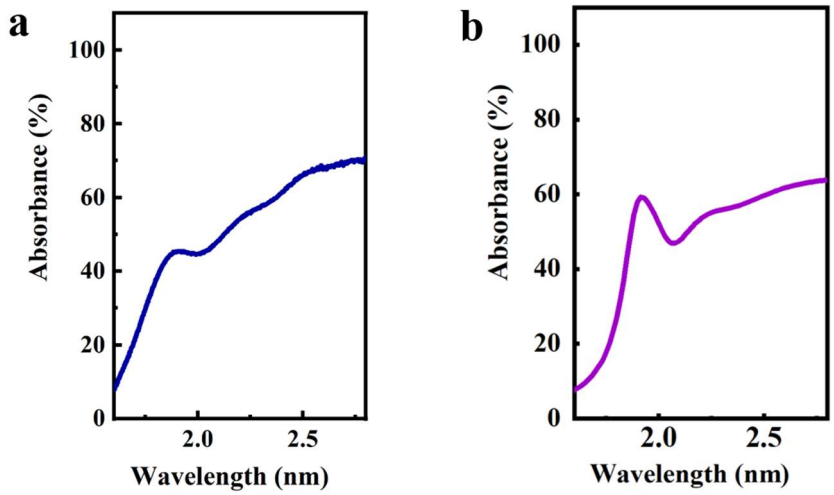

Figure S10. (a) Measured absorption spectrum of the AuNS91@PS-SH monolayer. (b) Simulated absorption spectrum of the AuNS91@PS-SH monolayer obtained from FDTD simulations. The experimental results show good agreement with the theoretical simulations. This agreement validates the accuracy of the optical model and the assumptions regarding nanoparticle size and spacing.

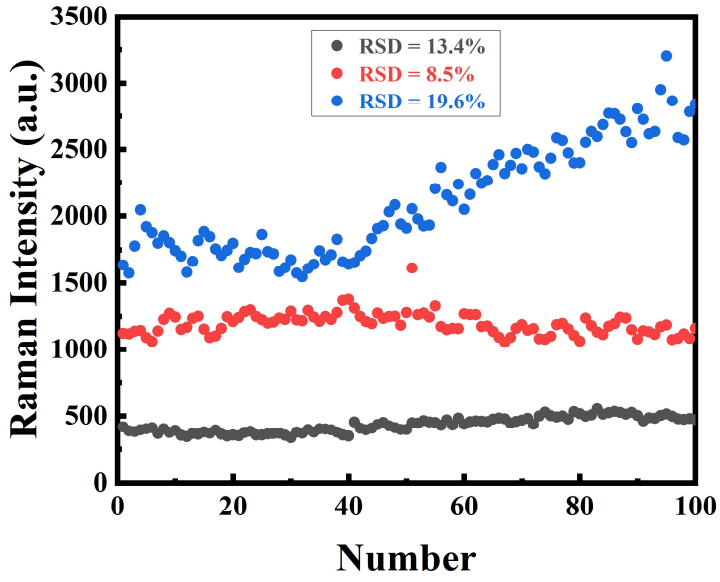

Figure S11. Schematic illustration of the signal reproducibility of the Raman peak at 592 cm^{-1} for different superlattices: AuNS68@PS-SH (gray), AuNS91@PS-SH (red), AuNS114@PS-SH (blue).

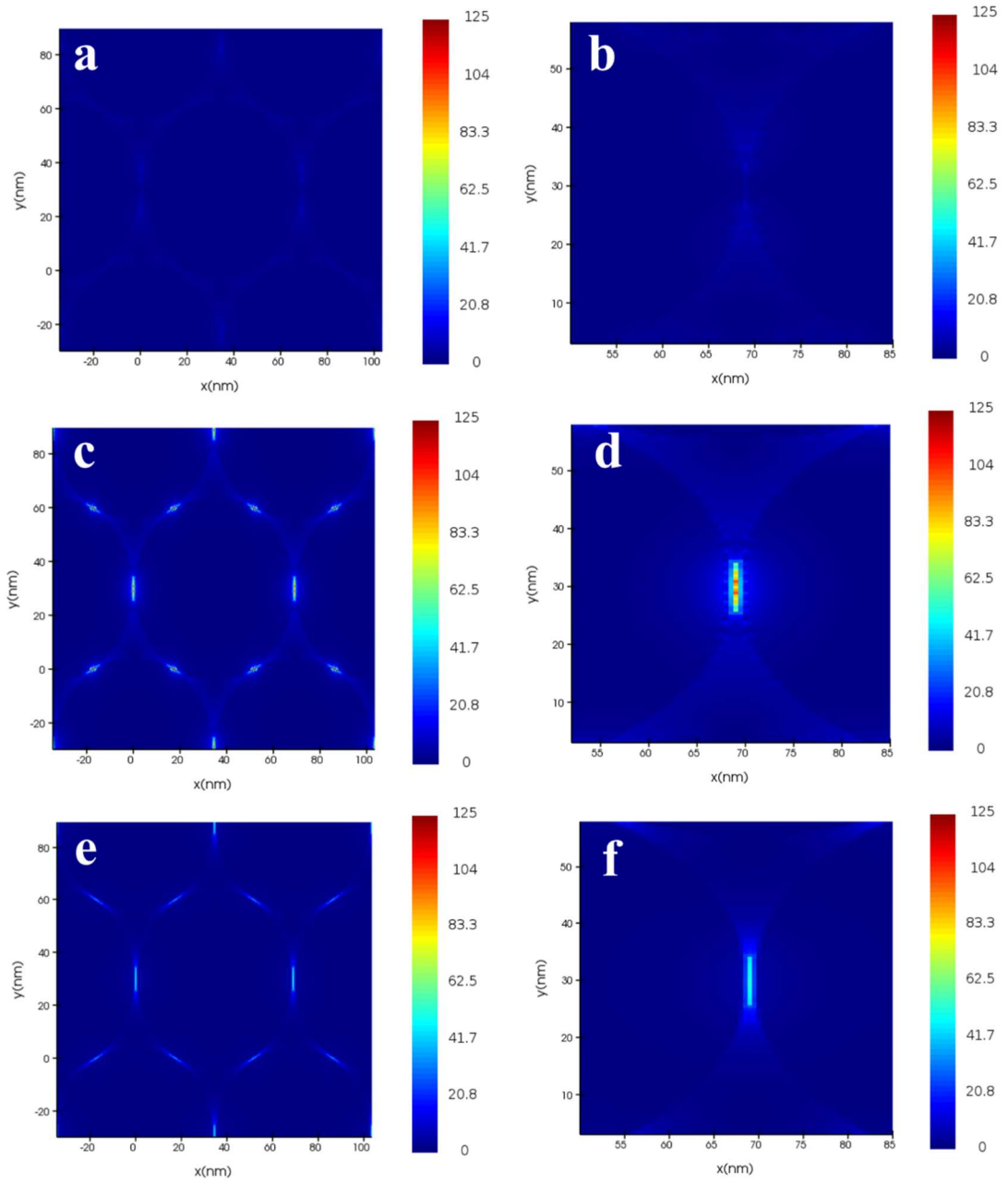

Figure S12. Near-field distribution of AuNS68@PS-SH superlattice under laser excitation with different wavelengths. (a, b) 785 nm, (c, d) 633 nm, and (e, f) 532 nm. Panels b, d, and f show magnified views of the near-field distributions presented in panels a, c, and e, respectively. Under laser excitations at wavelengths of 785 nm, 633 nm, and 532 nm, the maximum $|E/E_0|$ values are 11, 125, and 51, respectively. The images illustrate wavelength-dependent variations in near-field intensity, with stronger field enhancement observed near the plasmonic resonance wavelengths.

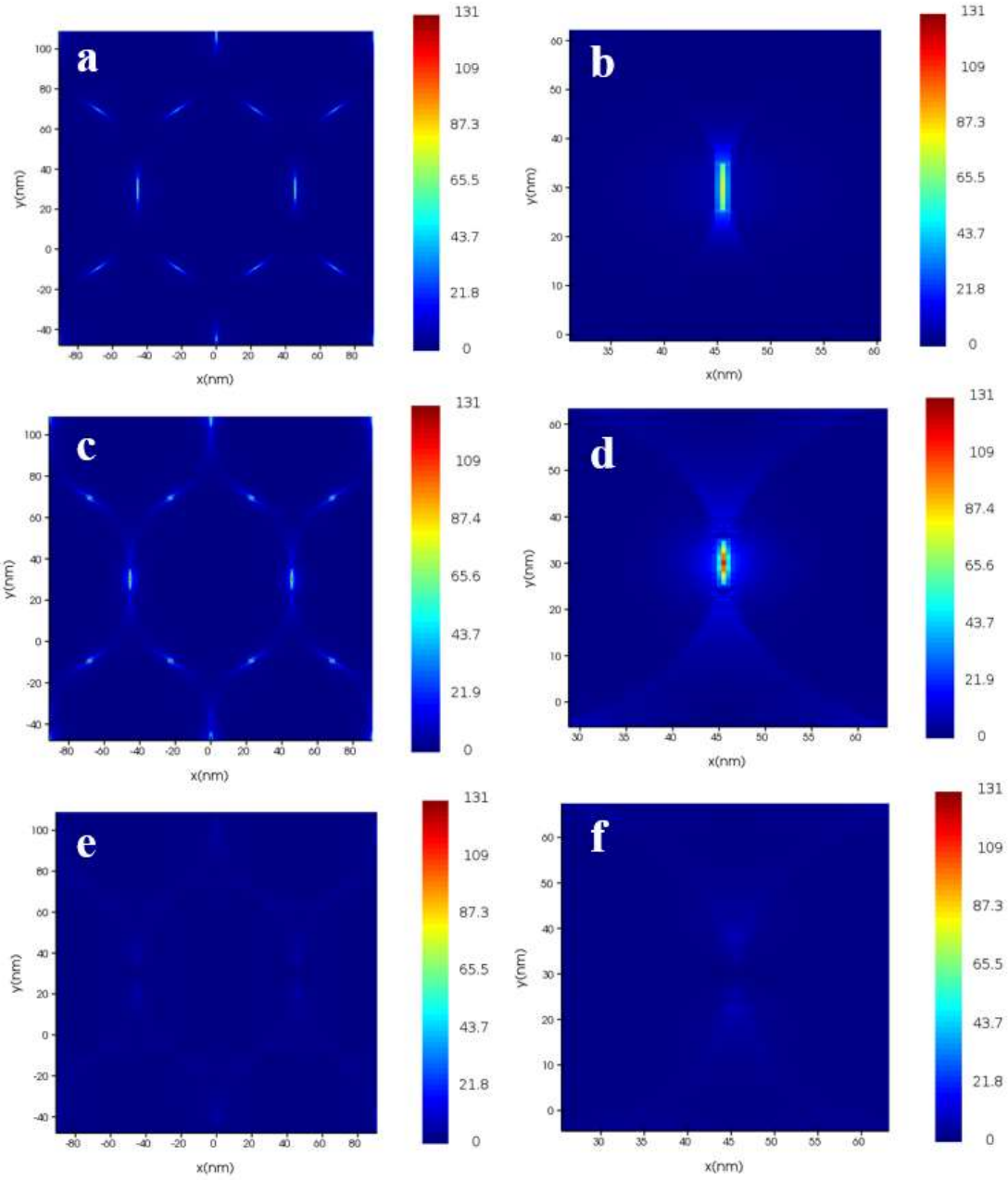

Figure S13. Near-field distribution of AuNS91@PS-SH superlattice under laser excitation with different wavelengths. (a, b) 785 nm, (c, d) 633 nm, and (e, f) 532 nm. Panels b, d, and f show magnified views of the near-field distributions presented in panels a, c, and e, respectively. Under laser excitations at wavelengths of 785 nm, 633 nm, and 532 nm, the maximum $|E/E_0|$ values are 61, 131, and 8, respectively. The images illustrate wavelength-dependent variations in near-field intensity, with stronger field enhancement observed near the plasmonic resonance wavelengths.

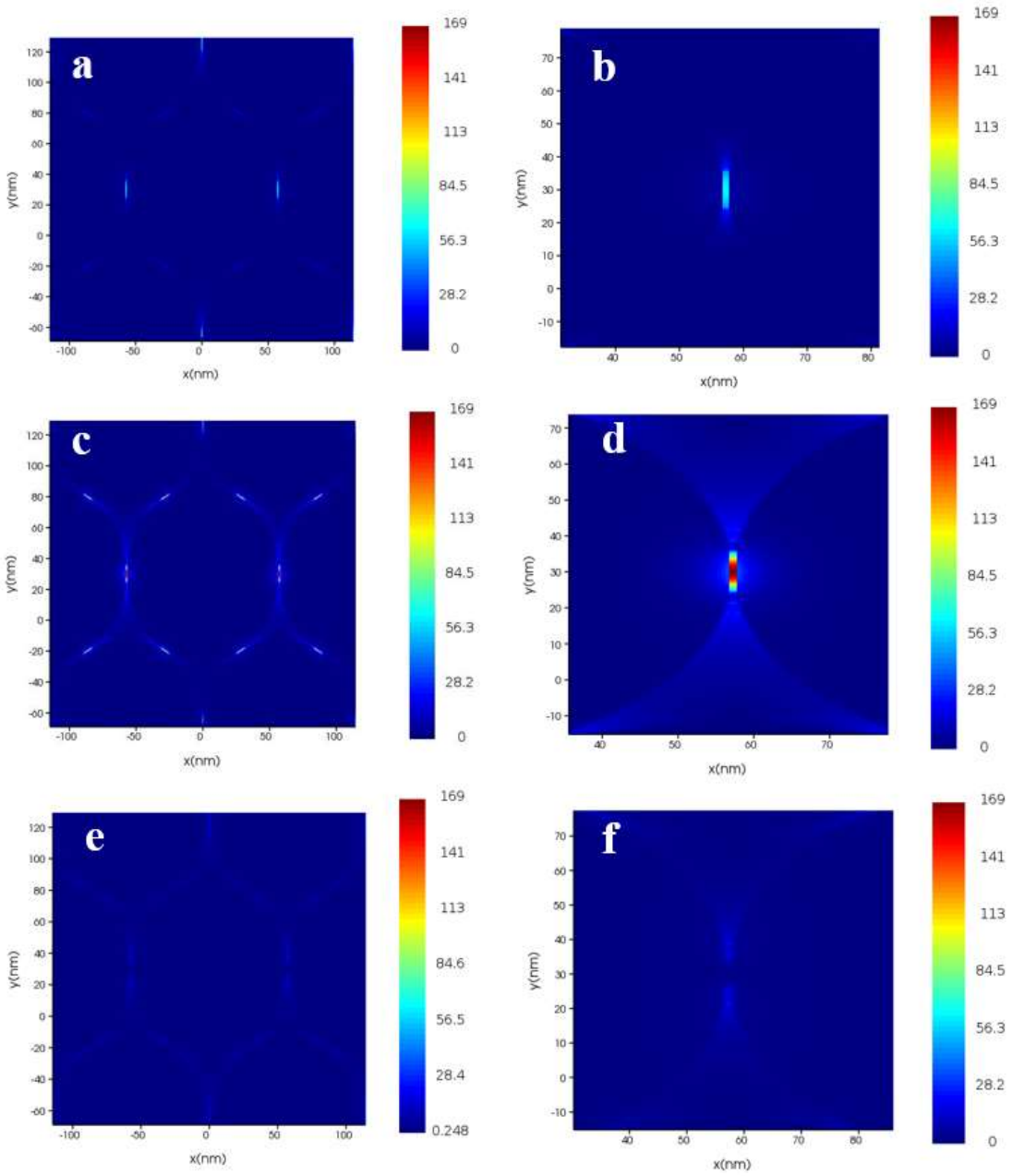

Figure S14. Near-field distribution of AuNS114@PS-SH superlattice under laser excitation with different wavelengths. (a, b) 785 nm, (c, d) 633 nm, and (e, f) 532 nm. Panels b, d, and f show magnified views of the near-field distributions presented in panels a, c, and e, respectively. Under laser excitations at wavelengths of 785 nm, 633 nm, and 532 nm, the maximum $|E/E_0|$ values are 70, 169, and 26, respectively. The images illustrate wavelength-dependent variations in near-field intensity, with stronger field enhancement observed near the plasmonic resonance wavelengths.